RSC Advances

PAPER

View Article Online
View Journal | View Issue

Cite this: *RSC Adv.*, 2026, **16**, 14566

Charge-transfer interactions govern the trans influence and electron-induced bond activation in linear Au(I) complexes

Akef T. Afaneh, *[a] Mansour H. Almatarneh, [bc] Ibrahim A. Daboubash,[a] Ali Marashdeh *[ad] and Oqab M. Abu Rumman[b]

Linear Au(I) complexes with the general formula of X–Au–L (X = Cl, Br, or I; L = OMe_2, SMe_2, $SeMe_2$, or $TeMe_2$) are model systems that exhibit trans influence and are directly relevant to focused electron-beam-induced deposition (FEBID), where low-energy electrons trigger precursor fragmentation. Using DFT/NBO together with ETS-NOCV/EDA and TD-DFT hole–electron analyses, we show that trends in Au–L bond strengthening and Au–X bond weakening are governed primarily by orbital-interaction/charge-transfer channels, including σ(Au–X)→σ*(Au–L) trans delocalization and ligand lone-pair donation into Au acceptor orbitals, which together modulate ΔE_{orb} and the Au–L Wiberg bond order. Electron-attachment thermodynamics identify the most favorable dissociation channels and define an electron-induced lability metric $G_{lab} \equiv -\Delta G_{frag,\ min}$, where $\Delta G_{frag,\ min}$ is the most favorable (most negative) fragmentation free energy. The overlap metric S_r provides a trigger proxy for localized low-threshold excitations. To integrate these observables without double-counting, we construct a parsimonious precursor viability index (PVI3), combining G_{lab} and interaction stabilization $S_{int} = -\Delta E_{int}$ as benefits and S_r as a penalty; ΔC and WBI are retained as mechanistic correlates rather than as independent score components. The resulting ranking highlights ClAu(S/Se)Me_2 as the most balanced candidate within this series, and this work provides a reproducible framework for FEBID-style screening.

Received 10th February 2026
Accepted 2nd March 2026

DOI: 10.1039/d6ra01199c

rsc.li/rsc-advances

Introduction

Predicting and rationalizing molecular stability, reactivity, and spectroscopic responses underpin advances from catalysis to nanofabrication. Frontier molecular orbitals (FMOs) offer a comprehensive understanding of these properties; however, in larger or highly polarizable systems, orbital delocalization can create difficulties in understanding which fragments control bond activation, charge transfer, or excited-state localization.[1–5] Fragment-aware descriptors and energy-decomposition analyses therefore provide a quantitative, fragment-resolved complement to FMO interpretations, particularly when both donor–acceptor interactions and Pauli repulsion contribute appreciably to bonding and response.

Gold is often described as a soft Lewis acid, and the linear, two-coordinate Au(I) motif is especially attractive due to its broad ligand tolerance and well-defined trans influence. In Au(I) halide adducts, X–Au–L (X = Cl, Br, or I; L = neutral donor), both experimental and computational results show that d(Au–X) increases, Au–X weakens and polarizability increases from Cl to I.[6–21] These complexes are also central to focused electron-beam-induced deposition (FEBID), in which adsorbed precursors are dissociated by low-energy electrons to directly fabricate metal nanostructures.[22–27] Gold FEBID remains compelling for plasmonic and electronic applications, but its progress hinges on the choice of the precursor: molecules must be stable enough for delivery while remaining sufficiently labile to fragment under the beam.[6–9,23,28–30]

In the present series of X–Au–L, electronegativity and polarizability covary for both X (Cl → Br → I) and L (O → S → Se → Te). Accordingly, we do not interpret any single HSAB "softness" metric as a standalone causal predictor. Instead, we interpret trends using decomposed computed observables, including CDA (charge-decomposition analysis) and NPA (natural population analysis) charge redistributions, as well as ETS–EDA (extended transition state energy-decomposition analysis) partitioning into ΔE_{elstat} (electrostatic interaction), ΔE_{Pauli} (Pauli/exchange repulsion), and ΔE_{orb} (the orbital-interaction/charge-transfer term), together with the dominant ETS-NOCV (ETS with natural orbitals for chemical valence) channels, thereby explicitly separating polarization, Pauli repulsion, and covalent/orbital interactions.

[a]*Department of Chemistry, Faculty of Science, Al-Balqa Applied University, 19117 Al-Salt, Jordan. E-mail: umafaneh@bau.edu.jo; a.marashdeh@bau.edu.jo*
[b]*Department of Chemistry, University of Jordan, Amman 11942, Jordan*
[c]*Department of Chemistry, College of Science, Imam Mohammad Ibn Saud Islamic University (IMSIU), Riyadh 11623, Saudi Arabia*
[d]*Leiden Institute of Chemistry, Gorlaeus Laboratories, Leiden University, Leiden, The Netherlands*

Here, we investigate how the anionic ligand X and neutral donor L modulate the ground- and excited-state electronic structure of linear X–Au–L complexes, and how these changes translate into FEBID-relevant trade-offs between precursor stability and electron-induced activation. We use DFT/NBO/EDA for ground states and TD-DFT for excited states to quantify fragment coupling, charge transfer (CT), and the balance among electrostatics, Pauli repulsion, and orbital interactions in the interaction energy (ΔE_{int}). We introduce a compact frontier descriptor, $\Delta C \equiv \mathrm{C\%(HOMO)_L} - \mathrm{C\%(LUMO)_L}$, and show its inverse relationship with the Au–L Wiberg bond order across the series (quantified in Results; see SI, TSI-7I). We also correlate the Au NBO (NPA) charge with the HOMO–LUMO gap, using Au charge as a simple electronic indicator of gap tuning, and we combine the hole–electron overlap metric S_{r} with the excitation energy E_{ex} to identify low-threshold, localized excitations relevant to electron-induced bond activation.

To translate these observables into FEBID precursor selection, we introduce a normalization-based precursor viability index (PVI). Because several candidate inputs—WBI(Au–L) (taken here as the NBO Wiberg bond index of the Au–L bond), the frontier-balance descriptor $\Delta C \equiv C_{\mathrm{L}}(\mathrm{HOMO}) - C_{\mathrm{L}}(\mathrm{LUMO})$ (where $C_{\mathrm{L}}(\psi)$ is the fraction or percentage of an orbital's AO weight residing on ligand AOs), and the electron-induced lability metric $G_{\mathrm{lab}} \equiv -\Delta G_{\mathrm{frag,min}}$—are strongly collinear within the present 12-complex dataset, the main-text score is formulated in a parsimonious, collinearity-aware form (PVI3) based on G_{lab} and $S_{\mathrm{int}} \equiv -\Delta E_{\mathrm{int}}$ as benefits and S_{r} as a penalty, while WBI(Au–L) and ΔC are retained as mechanistic correlates (see the PVI section and SI for diagnostics; SI. 8–10). Across the trans axis, σ(Au–X) → σ*(Au–L) delocalization provides a *trans*-coupling channel that attenuates the Au–X bond and tunes the Au–L interaction; this is quantified using NBO/Wiberg indices, ETS-NOCV/EDA, and CDA.

Prior studies of Au(I) bonding and trans influence have established qualitative trends with donor strength and halide type. Here we add three compact, operational elements aimed at FEBID-style screening: (i) a mechanistic ΔC–WBI relationship, linking ligand-referenced frontier balance to WBI(Au–L) across X–Au–L (used as an interpretation tool rather than an independent screening axis); (ii) a charge-transfer/orbital-interaction map, which shows that interaction trends are dominated by the orbital term ΔE_{orb} and its ETS-NOCV channels, rationalizing access to the σ(Au–X) → σ*(Au–L) *trans*-coupling pathway; and (iii) a collinearity-aware precursor-viability index used for ranking, reported as PVI3 in the main text and accompanied by a PC1-compressed sensitivity variant ($\mathrm{PVI_{PC}}$) in the SI (see SI, TSI-7A–TSI-7H).

Computational methods

All ground-state structures were optimized with Kohn–Sham DFT at the B3LYP level[31–33] using aug-cc-pVTZ for main-group atoms and aug-cc-pVTZ-PP (effective-core potentials) for Au, Te, and I.[34] Harmonic vibrational analyses at the same level confirmed each reported structure at its energy minimum (no imaginary modes). Unless otherwise stated, calculations were performed in the gas-phase; thermochemical corrections to Gibbs free energies employed the rigid-rotor harmonic-oscillator (RRHO) approximation at 298.15 K at the optimization level. All Gaussian runs used Gaussian 09.[35]

Vertical singlet excitations were computed by linear-response TD-DFT/TD-SCF[36,37] using CAM-B3LYP[13] with the same basis/ECP partitioning (aug-cc-pVTZ used on main-group atoms; aug-cc-pVTZ-PP used on Au, Te, and I) in the gas phase. For each complex, the lowest 20 singlet states were evaluated to characterize the near-UV/visible spectral manifold. Spin–orbit effects were assessed qualitatively on a representative subset using SOC-TDDFT (RI-SOMF) in ORCA 6.0 (ref. 38) at the same functional/basis level.[12,37,39] Scalar-relativistic effects for Au and I were treated using the effective-core potentials in aug-cc-pVTZ-PP (ref. 34); no additional DKH or ZORA corrections were applied in the Gaussian calculations.

Software and robustness checks. Unless otherwise stated, the full dataset reported in the main text was obtained at the levels described above (B3LYP/aug-cc-pVTZ(-PP) for ground-state optimizations and RRHO thermochemistry; CAM-B3LYP/aug-cc-pVTZ(-PP) for TD-DFT vertical excitations). Dispersion corrections were not included in the primary B3LYP dataset because the key observables in this work are intramolecular Au–X/Au–L bonding descriptors and charge-transfer metrics in small, rigid mononuclear complexes, for which empirical dispersion primarily affects the weak long-range methyl–methyl contacts and contributes to near-constant energetic offsets rather than altering relative trends. This assumption was supported by subset recomputations using dispersion-inclusive ωB97X-D/def2-TZVP (and D3(BJ), wherever applicable), which leave the rankings of ΔC_{norm}, WBI(Au–L), q_{Au}, and ΔE_{gap} unchanged (SI. 5; Tables TSI-10 and TSI-11). In addition, to assess functional/basis and code sensitivities, a representative subset was recomputed using CAM-B3LYP/def2-TZVP and ωB97X-D/def2-TZVP (Stuttgart/def2 ECPs for Au and halides; D3(BJ) where stated; ultrafine grids; tight SCF thresholds). For these cases, we reported (i) geometry optimizations and harmonic frequencies, (ii) NBO/NPA descriptors (WBI(Au–L), charges), and (iii) the lowest vertical singlet excitations. The ORCA 6.0 reproductions at identical settings confirmed code independence; differences remained within normal numerical tolerances, and all qualitative trends and rankings remained unchanged (see SI, robustness/validation; Table TSI-11).

Level of theory: selection and validation. Our workflow targets the achievement of both (i) reliable ground-state structures/thermochemistry for X–Au–L and (ii) a physically meaningful description of charge polarization and charge-transfer trends based on the CDA/EDA interpretation (see also the 'Software and robustness checks' section for the subset recomputations at def2-TZVP). For assessing ground-state geometries and vibrational thermochemistry, we employed hybrid DFT with triple-ζ basis sets and scalar-relativistic treatment appropriate for Au and the heavier halides; this protocol reproduced the established Au–X distance hierarchy (Cl < Br < I) and yielded Au–X and Au–L bond lengths within the expected accuracy window for Au(I) complexes, with a modest systematic positive bias that does not affect relative trends. For the electronic-structure analyses that considerably

depend on donor/acceptor polarization (frontier-orbital projections, CDA CT channels, and related descriptors), we used CAM-B3LYP because its range separation mitigates delocalization error and the spurious stabilization of charge-transfer states that can occur with conventional hybrids, thereby providing a more robust basis for comparing X → AuL *versus* L → AuX polarization across O/S/Se/Te. Scalar-relativistic effects were included consistently *via* the employed ECPs, as specified above. Dispersion was not applied to the primary B3LYP dataset; however, its impact was assessed through dispersion-inclusive subset recomputations (ωB97X-D and, where stated, D3(BJ)), confirming that the qualitative rankings and correlations discussed in the text were unchanged (SI. 5; Tables TSI-10 and TSI-11).

Bonding and population analyses used NBO 3.1 (ref. 40) (as interfaced in Gaussian) to obtain Wiberg bond indices (WBI) and second-order donor → acceptor stabilization energies; atomic charges were obtained from the natural population analysis (NPA) section of the NBO output. Multiwfn 3.8 (ref. 41) was used for real-space hole–electron analysis to compute the overlap metric S_r and fragment population decompositions. For the frontier-balance descriptor, the ligand contribution to a molecular orbital ψ is defined as $C_{L(\psi)} = 100 \times \frac{\sum_{\mu\in L}(c_\mu)^2}{\sum_{\mu\in \text{all}}(c_\mu)^2}$, where c_μ are MO coefficients in the AO basis, and the numerator sums AOs on the ligand fragment L. We define $\Delta C \equiv C_L(\text{HOMO}) - C_L(\text{LUMO})$ and report it in Table 1 as the difference in ligand contribution between the HOMO and LUMO. In the present 12-complex series, ΔC was retained primarily for mechanistic interpretation (and shown alongside WBI and fragmentation thermodynamics), but it was not treated as an independent ingredient in the main-text PVI3 ranking due to descriptor collinearity (SI. 9). Bond order between the EDA fragments F1 = XAu and F2 = L was reported as an interfragment Wiberg bond index, computed by summing NBO Wiberg indices over all atom pairs across the two fragments: $\text{WBI}(\text{F1}\|\text{F2}) = \sum_{A\in \text{F1}}\sum_{B\in \text{F2}} \text{WBI}_{AB}$. For the present linear monodentate X–Au–L series, this interfragment index was numerically dominated by (and effectively equivalent to) Au–Y WBI (Y = donor atom); hence, we also refer to it as WBI(Au–L) for brevity.

Energy-decomposition analyses followed the Morokuma–Ziegler partitioning (ΔE_{elstat}, ΔE_{Pauli}, ΔE_{orb}, ΔE_{disp}) and were carried out as ETS-NOCV in ORCA 6.0 (ref. 38) using neutral singlet fragments F1 = XAu ($S = 0$) and F2 = L ($S = 0$) unless stated otherwise. Charge-decomposition/ETS-NOCV charge-flow analyses were evaluated in both directions (X → Au–L and L → Au–X).[42–44] For comparison with conceptual-DFT reactivity indices, we evaluated the ligand-condensed dual descriptor $\Delta f = f^+ - f^-$, where f^+ and f^- are the condensed Fukui functions for nucleophilic and electrophilic attack, respectively, summed over the ligand atoms, following Morell, Grand, and Toro-Labbé.[45] To compare Au–L and Au–X bond lengths across donors/halides of different sizes, we calculated size-normalized distances $d_{\text{norm}}(\text{Au}-\text{Y}) = \frac{d(\text{Au}-\text{Y})}{R_{\text{cov(Au)}} + R_{\text{cov(Y)}}}$ (Y = L or X) using covalent radii from Cordero *et al.*[46] to define the bond-distance cutoff (*i.e.*, atoms were considered bonded when $d_{AB} \le r_{\text{cov}}(A) + r_{\text{cov}}(B)$ [±tolerance, if you used one]); the radii and resulting d_{norm} values are tabulated in the SI (TSI-8).

Neutral bond-dissociation Gibbs free energies, $\Delta_{BD}G$, were evaluated as adiabatic RRHO Gibbs free-energy changes at 298.15 K for X–Au–L → X + AuL (and related neutral channels), with all species optimized at the B3LYP/aug-cc-pVTZ(-PP) level (with aug-cc-pVTZ-PP ECPs for Au and I); electron-induced fragmentation free energies, ΔG_{frag}, were analogously defined for X–Au–L + e^- → $[\text{X–Au–L}]^-$, followed by dissociation to the indicated fragments. Unless otherwise noted, ΔG_{frag} values reported in Table 3 correspond to the adiabatic thermochemical cycle (optimized $[\text{X–Au–L}]^-$ and optimized fragments prior to RRHO free-energy evaluation) and do not include a separate vertical (fixed-geometry) attachment step. Charge/multiplicity conventions, definitions of vertical *versus* adiabatic steps, and the treatment of spin–orbit coupling (SOC) for Au/I (where applicable) are documented in the SI (SI. 4; Tables TSI-14 and TSI-15), together with the Cartesian coordinates and representative input files (SI. 6). Transition-state (TS) searches were attempted for relevant substitution/dissociation steps using the QST2/QST3 and TS optimizations seeded from relaxed coordinate scans at the same level of theory used for the corresponding energy minima; however, no converged first-order saddle point (single imaginary frequency) was obtained for any complex, with candidate optimizations relaxing to nearby energy minima or failing to converge on a shallow potential-energy surface. Accordingly, we did not report TS-derived activation parameters; the mechanistic discussion was restricted to scan-guided qualitative trends and the relative stability of the identified energy minima, and $|\Delta G_{\text{frag}}|_{\text{min}}$ was used as a thermodynamic proxy for scission propensity in the PVI analysis (SI. 4).

Table 1 Ligand frontier-orbital contributions (HOMO/LUMO), ΔC, and WBI(F1‖F2)[a]

	FO contribution (C%)			
	HOMO	LUMO	ΔC	WBI(F1‖F2)
OMe_2	96.3 (96.5) [96.8]	3.7 (3.5) [3.2]	92.60 (93.00) [93.60]	0.328 (0.294) [0.209]
SMe_2	81.3 (84.7) [84.9]	18.8 (15.4) [17.1]	62.50 (69.30) [67.80]	0.459 (0.422) [0.336]
$SeMe_2$	78.2 (78.8) [79.9]	21.9 (21.1) [20.2]	56.30 (57.70) [59.70]	0.468 (0.426) [0.366]
$TeMe_2$	73.6 (74.3) [75.7]	26.3 (25.8) [24.1]	47.30 (48.50) [51.60]	0.590 (0.553) [0.491]

[a] For each ligand L, values are reported as ClAuL (BrAuL) [IAuL].

Precursor viability index (PVI). To rank the X–Au–L candidates for FEBID-style screening, we combined the computed descriptors into a precursor viability index (PVI). In this chemically narrow 12-complex series, three descriptors – WBI(Au–L), the frontier-balance descriptor ΔC, and the electron-induced fragmentation/lability metric – were strongly collinear; using all three as independent components in a single additive score would therefore double-count the same underlying "lability/activation" trend. For this reason, the main-text ranking used a parsimonious, collinearity-aware index (PVI3) built from three less-redundant criteria: (i) the electron-induced lability benefit, $G_{lab} \equiv -\Delta G_{frag,\ min}$, where $\Delta G_{frag,\ min}$ was the most favorable (the most negative) fragmentation free energy among the considered channels; (ii) the interaction stabilization $S_{int} = -\Delta E_{int}$ (benefit); and (iii) the S_r metric (penalty). WBI(Au–L) and ΔC were retained in Tables 1 and 4 and discussed mechanistically, but they were not treated as independent score components in PVI3.

All metrics were mapped onto a common [0,1] scale using min–max normalization over the full set of complexes: $Z_m^j = \frac{m^{(j)} - m_{min}}{m_{max} - m_{min}}$; $m_{min} = \min_k m^{(k)}$ and $m_{max} = \max_k m^{(k)}$. For penalty metrics (S_r), we used the transformed contribution $(1 - z_m^{(j)})$ so that the larger values always indicated a more promising precursor. The resulting three-term index was $PVI3^{(j)} = \frac{zG_{lab}^{(j)} + zS_{int}^{(j)} + (1 - zS_r^{(j)})}{3}$, which lies between 0 and 1 because each z-score is min–max normalized to [0,1] and the expression is the average of three terms in [0,1].

For transparency, we also calculated the original five-term index (PVI5), which combined the delivery- and lability-relevant descriptors using fixed weights. Benefit terms were entered as $z_m^{(j)}$, whereas penalty terms were entered as $(1-z_m^{(j)})$. Using WBI(Au–L), G_{lab}, and S_{int} as benefits and ΔC and S_r as penalties, we defined $PVI5 = 0.25\ z_{BO}{}^j + 0.20\ (1 - z_{\Delta C}{}^j) + 0.20\ z_{|\Delta G|}{}^j + 0.20\ (1 - z_{S_r}{}^j) + 0.15\ z_{S_{int}}{}^j$. As ΔC, WBI(Au–L), and G_{lab} were strongly collinear within this series, PVI5 was provided mainly for transparency and sensitivity checks (SI), together with a PC1-compressed variant (PVI_{PC}); these checks do not change the qualitative conclusions for the present dataset.

Results and discussion

Across the donor series L = OMe_2 → SMe_2 → $SeMe_2$ → $TeMe_2$, the Au–L interaction strengthens electronically even though the direct Au–L distance increases with the donor size. Because direct distances conflate size with bonding, we consider the size-normalized contact metric d_{norm}(Au–Y) = d(Au–Y)/[R_{cov}(Au) + R_{cov}(Y)] (covalent radii from Cordero *et al.*; SI: TSI-8)[46] only as a geometric comparator and do not use it to infer covalency. Instead, electronic strengthening is assessed using Wiberg bond indices (WBI from NBO) and ETS-EDA/ETS-NOCV descriptors, in particular the orbital-interaction/charge-transfer term ΔE_{orb} and dominant NOCV channels (SI: TSI-16A, B).[42–44] Using these

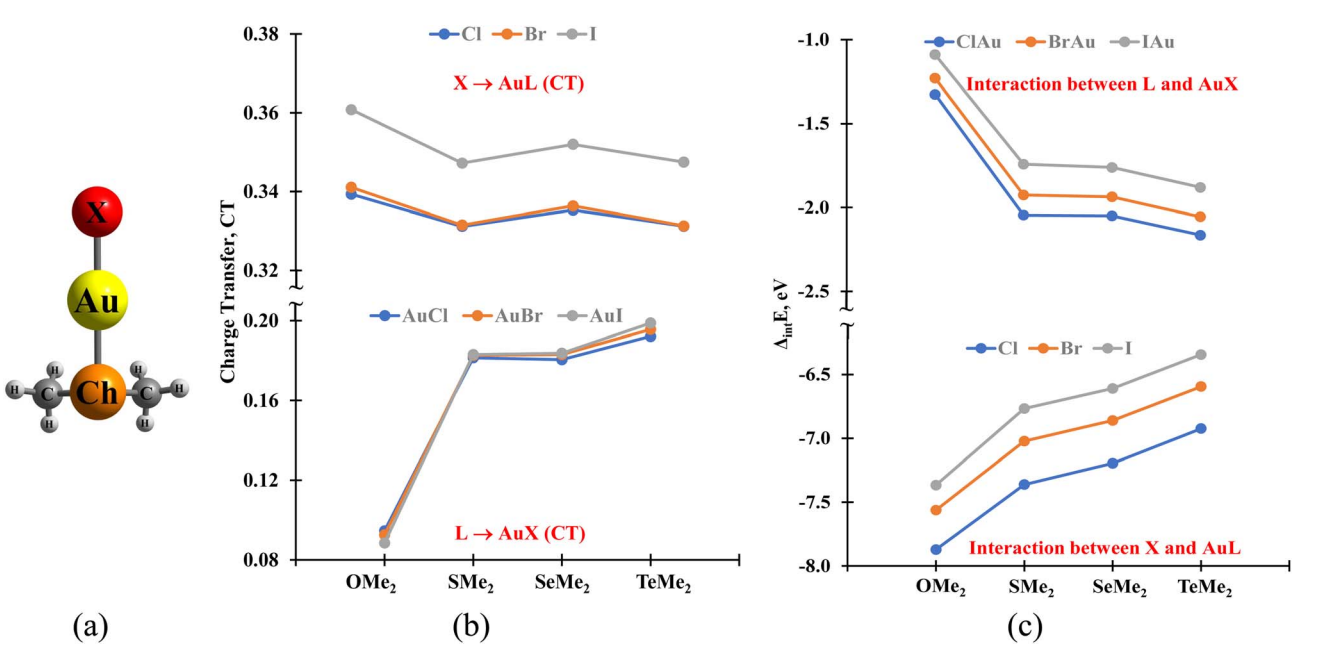

Fig. 1 (a) Representative linear topology and fragment partitioning used in the CDA/EDA analyses for X–Au–L (X = Cl, Br, or I; L = $ChMe_2$ with Ch = O, S, Se, or Te). (b) Charge-decomposition analysis (CDA), showing the net charge-transfer terms (CT magnitudes are reported; arrows denote direction) as a function of ligand identity L (abscissa: OMe_2 → SMe_2 → $SeMe_2$ → $TeMe_2$). The upper subpanel reports the X → AuL CT term, and the lower subpanel reports the L → AuX CT term. (c) Energy-decomposition analysis (EDA), showing the pairwise interaction energies between fragments (ΔE_{int}, eV; more negative indicates stronger stabilization) plotted against the same abscissa (L = OMe_2, SMe_2, $SeMe_2$, or $TeMe_2$). The upper subpanel shows the interaction between L and AuX, and the lower subpanel shows the interaction between X and AuL. Legends indicate the halide X. The numerical values underlying panels (b) and (c) are tabulated in the SI (CT terms: Table TSI-3; EDA interaction term used in the analysis, $S_{int} = -\Delta E_{int}$: Table TSI-12). Complete molecular schematics for all X/L combinations are provided in Fig. SI. 1.

observables, both WBI(Au–L) and ΔE_{orb} increase from OMe_2 to heavier chalcogen donors, indicating enhanced electronic coupling, while ΔE_{int} reflects the balance among electrostatics, Pauli repulsion, and orbital contributions. In parallel, σ(Au–X) → σ*(Au–L) delocalization provides a *trans*-coupling pathway that decreases Au–X bonding and adjusts Au–L bonding, consistent with the classical trans influence in linear d^{10} Au(I) complexes.[21,39,47] Detailed structural benchmarks and full geometric trends are provided in the SI (SI. 1).

Charge-decomposition analysis (CDA) and ETS-EDA map fragment coupling by relating CT(L → XAu) to the interaction energy ΔE_{int}(XAu‖L)[42–44]

Across OMe_2 → SMe_2 → $SeMe_2$ → $TeMe_2$ at fixed X, CT increases, and the interaction becomes more stabilizing; across Cl → Br → I at fixed L, stabilization is generally attenuated. Within this dataset, the orbital-interaction term (ΔE_{orb}), which captures donor–acceptor mixing/CT, tracks the overall interaction energy most closely (Pearson $r(\Delta E_{int}, \Delta E_{orb}) = 0.980$, $R^2 = 0.960$, $N = 12$; SI Table TSI-16A; see also TSI-7I), while ΔE_{elstat} and $\Delta E_{Pauli,total}$ are strongly anti-correlated ($r = -0.984$, $R^2 = 0.969$, $N = 12$; SI Table TSI-16A; see also SI Table TSI-7I) and therefore partially cancel one another, so their combined contribution varies more weakly across the series than either term individually. Accordingly, we treat CT/ΔE_{orb} as a decisive contribution when rationalizing trends and avoid over-interpreting individual electrostatic or Pauli components in isolation.[13,15,16,41,48] The observed increase in WBI(Au–L) cannot be attributed to increased occupation of σ*(Au–L), because donation into σ*(Au–L)-for example *via* a σ(Au–X) → σ*(Au–L) charge-transfer pathway-would weaken the Au–L bond rather than strengthen it. The net increase arises from enhanced *n*(Ch) → Au covalency (more negative ΔE_{orb}), which dominates over the *trans*-weakening channel (Fig. 1).

A compact, EDA-independent descriptor, ΔC, is defined from ligand frontier-orbital contributions as $\Delta C \equiv C_L(\text{HOMO}) - C_L(\text{LUMO})$, where $C_L(\psi)$ is the fraction (or percentage) of the AO-weight of orbital ψ residing on ligand AOs (see the Computational methods section); C_L(HOMO) and C_L(LUMO) are reported in Table 1. Across the X–Au–L series, a larger ΔC coincides with a smaller WBI(F1‖F2), whereas a smaller ΔC accompanies larger WBI: OMe_2 exhibits the largest ΔC and smallest WBI, while $TeMe_2$ shows the smallest ΔC and largest WBI (Pearson $r = -0.881$, $R^2 = 0.776$, $N = 12$; see SI, TSI-7I). Thus, smaller ΔC signals more balanced ligand participation at the frontier level and tighter electronic coupling, consistent with the strengthening observed along O → S → Se → Te. Importantly, within this chemically narrow 12-complex set, ΔC is strongly collinear with other lability proxies (*e.g.*, G_{lab} and WBI); therefore, ΔC is used here primarily as a mechanistic frontier-localization indicator rather than as an independent component in the main-text PVI3 ranking (see SI).

Time-dependent DFT provides orthogonal cues relevant to FEBID

Within a given chemical subset, lower excitation energies often coincide with larger hole–electron overlap (S_r), reflecting more localized X–Au–L excitations (Pearson $r = -0.646$, $R^2 = 0.417$, $N = 12$; see SI, TSI-7I).[13,36,41] Because E_{ex} and S_r are spectroscopic descriptors rather than thermodynamic metrics, we do not equate them directly with stability. OMe_2 complexes deliberately deviate by displaying more metal- or halide-centered excitations, explaining why Au–X *versus* Au–L scission propensity can switch across X. As a trigger heuristic, larger S_r at lower E_{ex} suggests lower activation thresholds and a greater likelihood of populating dissociative channels under low-energy electron impact (Table 2).

Table 2 Excitation energy (E_{ex}) and hole–electron overlap (S_r)

Complexes	E_{ex}	S_r	Complexes	E_{ex}	S_r
$ClAuOMe_2$	6.547	0.512	$ClAuSeMe_2$	6.627	0.502
$BrAuOMe_2$	6.470	0.637	$BrAuSeMe_2$	6.428	0.507
$IAuOMe_2$	6.265	0.504	$IAuSeMe_2$	6.238	0.539
$ClAuSMe_2$	7.178	0.468	$ClAuTeMe_2$	6.466	0.613
$BrAuSMe_2$	6.831	0.475	$BrAuTeMe_2$	6.275	0.614
$IAuSMe_2$	6.425	0.567	$IAuTeMe_2$	5.911	0.631

To quantify how the lowest excitation redistributes density between the Au–X and Au–L sides of the complex, we analyzed the corresponding NTO hole/electron densities using two complementary fragment partitions: (XAu)|(L) and (X)|(AuL) (SI, TSI-3). In the (X)|(AuL) partition, the particle NTO density on X is generally minor-to-moderate (typically <20%, maximum 25.5%), indicating that the lowest excitation is not dominated by the σ*(Au–X) character but by a measurable σ*(Au–X)-like (X-involving) acceptor admixture. Notably, $BrAuOMe_2$ shows the strongest halide participation (25.5% on Br), consistent with our observation that OMe_2 can display more metal-/halide-involved low-energy excitations along with the reported switching of Au–X *versus* Au–L scission propensity across X. This excited-state partitioning is independent of the ground-state bond-length trends discussed above, which arise from the *trans*-axis CT/orbital-interaction effects in S0.

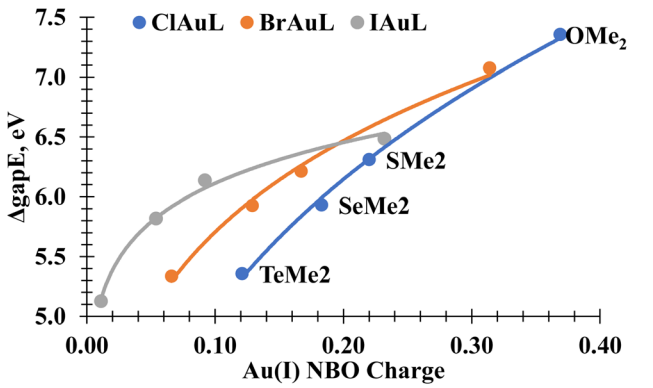

Fig. 2 HOMO–LUMO gap *versus* Au NBO (NPA) charge for X–Au–L. Along Cl → Br → I, the decreasing electronegativity reduces charge polarization toward X; therefore, EDA and CDA/NPA are used to separate polarization from covalency and Pauli contributions. Symbols are computed values for each halide series; solid lines are guides to the eye and are not mechanistic fits (Pearson $r = 0.922$; $R^2 = 0.851$; $N = 12$).

Table 3 Electron-induced fragmentation Gibbs free energies, ΔG_{frag} (298.15 K; eV), for X–Au–L + e^- → [X–Au–L]$^-$ → fragments. Values are thermodynamic driving forces (not activation barriers); negative ΔG_{frag} indicates an exergonic electron-induced dissociation channel. All ΔG_{frag} values in Table 3 are adiabatic (geometry relaxation after attachment is included). Charge/multiplicity conventions and protocol details are given in SI. 4 and Table TSI-14; TS-search outcomes are summarized in Table TSI-15

Reaction scheme: X–Au–L + e^- → [X–Au–L]$^-$ → fragments (channels listed below)[a]

Fragmentation channel (products)	OM_2	SMe_2	$SeMe_2$	$TeMe_2$
$ClAu^-$ + L	−1.678	−0.970	−0.896	−0.767
$BrAu^-$ + L	−1.751	−1.073	−0.995	−0.862
IAu^- + L	−1.831	−1.200	−1.118	−0.981
Cl^- + AuL	−0.459	−0.096	−0.122	−0.159
Br^- + AuL	−0.581	−0.248	−0.270	−0.302
I^- + AuL	−0.675	−0.389	−0.408	−0.436
Cl^- + Au + L	−0.658	0.050	0.124	0.252
Br^- + Au + L	−0.780	−0.102	−0.024	0.109
I^- + Au + L	−0.874	−0.243	−0.162	−0.024

[a] All-channels conserve total charge (−1) after electron attachment; *e.g.*, "$ClAu^-$ + L" denotes dissociation into an anionic Au–X fragment and neutral ligand, while "X^- + AuL" denotes the halide loss with a neutral AuL fragment. Channel definitions follow SI. 4 (Table TSI-9).

A gap–charge coupling (Fig. 2) emerges when the HOMO–LUMO gap, E_{gap}, is plotted against the Au(I) NPA charge q_{Au}. For a fixed ligand L, the halide series Cl → Br → I shows a monotonic decrease in both q_{Au} and E_{gap}, consistent with the increased Au–X covalency and charge redistribution. Across the donor series, at fixed X, OMe_2 lies at the high-q_{Au}/high-E_{gap} end, while S/Se/Te progressively reduce q_{Au} and compress E_{gap} as donor polarizability increases (and electronegativity decreases) and Au–L covalency increases. Thus, OMe_2 is not anomalous in trend direction; it is offset relative to the chalcogen donors, and the smaller E_{gap} is associated with a less cationic Au center and a higher reactivity potential.

Fragmentation windows for neutral channels ($\Delta_{BD}G$, 298 K) indicate that at a fixed halide, heavier chalcogens generally yield less favorable neutral dissociation, while at a fixed ligand, moving from Cl to I tends to make electron-induced fragmentation more exergonic. For electron-impact conditions relevant to FEBID, we report electron-induced fragmentation free energies, ΔG_{frag} (298 K), for X–Au–L + e^- → [X–Au–L]$^-$ → fragments (Table 3). Consistent with prior dissociative electron-attachment studies that have reported preferential Au–Cl scission upon electron attachment,[15] the ClAuL members of our set display strongly exergonic Au–Cl cleavage channels in the anionic fragmentation thermodynamics (Table 3; SI TSI-9). Because first-order saddle points could not be located for the corresponding substitution/dissociation pathways (SI. 4; TSI-15), we do not report TS-derived activation parameters; instead, the magnitude of the most exergonic channel, G_{lab}, is used as the thermodynamic proxy for scission propensity.

To summarize the screening outcomes, we report a precursor viability index, PVI, constructed from min–max normalized descriptors. In the main text, we use the parsimonious, collinearity-aware PVI3 (G_{lab} and S_{int} as benefits, S_r as a penalty), while WBI(Au–L) and ΔC are reported alongside the score as mechanistic correlates (Table 4). Full component tables and sensitivity checks (including the original five-term PVI5) are provided in the SI.

Within each halide or ligand subgroup, the descriptor values are internally consistent and highlight the same qualitative trade-offs (increasing WBI(Au–L) along O → S → Se → Te, while the net interaction stabilization S_{int} can be moderated by countervailing the terms in EDA).

These outcomes translate into three practical implications for FEBID precursor selection. First, coupling balance is captured by the joint behavior of ΔC and WBI: WBI(F1‖F2) is larger and XAu‖L coupling is stronger when the ligand contributes more evenly to HOMO and LUMO (smaller ΔC); thus, a full EDA decomposition is not required to obtain a first-pass trans influence diagnostic.[49–51] Second, the E_{gap}–q_{Au} relationship (HOMO–LUMO gap *versus* Au NPA charge) is used only as a qualitative frontier/hardness proxy and is interpreted alongside fragment-resolved observables (CDA/NBO/ETS-NOCV) that explicitly separate polarization and covalency.

Table 4 Descriptor summary and PVI3 ranking for X–Au–L complexes. Benefits are G_{lab} and $S_{int} = -\Delta E_{int}$; S_r is treated as a penalty *via* $(1 - z_{S_r})$. WBI(Au–L) and ΔC are reported as mechanistic correlates but are not included as independent PVI3 terms. Rank 1 is most promising within this series

Rank (PVI3)	Complexes	X	L	ΔC	WBI(Au–L) = WBI(F1‖F2)	G_{lab} (eV)	S_r	S_{int} (eV)	PVI3
1	$ClAuSMe_2$	Cl	SMe2	62.56	0.459	1.349	0.468	7.362	0.829
2	$ClAuSeMe_2$	Cl	SeMe2	56.28	0.468	1.424	0.502	7.195	0.747
3	$BrAuSMe_2$	Br	SMe2	69.28	0.422	1.228	0.475	7.023	0.705
4	$ClAuOMe_2$	Cl	OMe2	92.57	0.328	0.643	0.512	7.872	0.646
5	$BrAuSeMe_2$	Br	SeMe2	57.69	0.426	1.306	0.507	6.861	0.630
6	$ClAuTeMe_2$	Cl	TeMe2	47.33	0.590	1.553	0.613	6.924	0.507
7	$IAuOMe_2$	I	OMe2	93.67	0.209	0.419	0.504	7.366	0.485
8	$IAuSeMe_2$	I	SeMe2	59.76	0.366	1.131	0.539	6.609	0.460
9	$IAuSMe_2$	I	SMe2	65.76	0.336	1.050	0.567	6.768	0.416
10	$BrAuTeMe_2$	Br	TeMe2	48.51	0.553	1.439	0.614	6.595	0.400
11	$BrAuOMe_2$	Br	OMe2	93.00	0.294	0.549	0.637	7.563	0.304
12	$IAuTeMe_2$	I	TeMe2	51.62	0.491	1.269	0.631	6.344	0.262

Finally, electron triggering is assessed using the thermodynamic lability metric G_{lab} together with S_r and E_{ex}: larger S_r at lower E_{ex} indicates localized, low-threshold excitations that are more likely to yield bond-selective scission upon electron impact, while G_{lab} screens out overly exergonic fragmentation that could compromise delivery stability. In the collinearity-aware PVI3 ranking (Table 4), G_{lab} and S_{int} provide the primary balance between lability and robustness, with S_r acting as a conservative trigger penalty.

Conclusion

The bonding- and electron-induced reactivities in linear Au(I) complexes, X–Au–L, are significantly affected by the identities of the ligands and halides. The electron density at Au increases as the donor transitions from OMe_2 to $TeMe_2$. Delocalization along the trans axis (*e.g.*, σ(Au–X) → σ*(Au–L)) contributes to Au–X weakening and represents a trans influence (antibonding) channel that would, in isolation, oppose Au–L strengthening. The observed net strengthening of Au–L along the donor series is instead reflected by increased WBI/WBI (Au–L) and more stabilizing ΔE_{orb} from ETS-EDA/ETS-NOCV. The CT–ΔE_{int} quadrant map facilitates the categorization of fragment-pairing regimes, while energy-decomposition analysis elucidates the contributions of orbital interactions, electrostatics, and Pauli repulsion in defining ΔE_{int}. Ligand involvement in HOMO and LUMO is linked to bond order and coupling strength, ΔC, which serves as a small frontier descriptor that characterizes trans influence patterns. In FEBID, excited-state descriptors provide distinct insights: an increased S_r at reduced E_{ex} suggests a more direct pathway to dissociative channels, influenced by the thermodynamic window indicated by G_{lab}. We introduce a simple index that ranks precursors using only the reported tabulated descriptors, after scaling each descriptor by min–max normalization to enable consistent combination. This index outlines the process for actualizing these concepts and highlights the primary design requirement of FEBID: molecules must possess sufficient fragility for disintegration while maintaining adequate stability for delivery. Furthermore, it provides a systematic list of options and experimental variables that can influence the deposition outcomes, including dose, duration, temperature, and co-reactants.

Conflicts of interest

There are no conflicts to declare.

Data availability

The data supporting this study are available within the article and its supporting information (SI). Optimized Cartesian coordinates, computed descriptors (NBO charges, Wiberg bond indices, ΔC, and HOMO–LUMO gaps), and ETS-EDA/ETS-NOCV energy-decomposition data (including dominant NOCV channel populations and energies) are provided in the SI Tables (*e.g.*, TSI-16A and TSI-16B) and associated SI sections. Additional raw input/output files (Gaussian/ORCA job files) are available from the corresponding author upon reasonable request. Supplementary information is available. See DOI: https://doi.org/10.1039/d6ra01199c.

References

1 R. B. Woodward, and R. Hoffmann, *The Conservation of Orbital Symmetry*, Elsevier, 2013.
2 I. Fleming, *Molecular Orbitals and Organic Chemical Reactions*, John Wiley & Sons, 2011.
3 R. G. Parr and W. Yang, Density functional approach to the frontier-electron theory of chemical reactivity, *J. Am. Chem. Soc.*, 1984, **106**, 4049–4050.
4 I. Fleming, *Frontier Orbitals and Organic Chemical Reactions*, Wiley, 1977.
5 K. Fukui, T. Yonezawa and H. Shingu, A molecular orbital theory of reactivity in aromatic hydrocarbons, *J. Chem. Phys.*, 1952, **20**, 722–725.
6 G. Pakeltis, Z. Hu, A. G. Nixon, E. Mutunga, C. P. Anyanwu, C. A. West and P. D. Rack, Focused electron beam induced deposition synthesis of 3d photonic and magnetic nanoresonators, *ACS Appl. Nano Mater.*, 2019, **12**, 8075–8082.
7 W. G. Carden, R. M. Thorman, I. Unlu, K. A. Abboud, D. H. Fairbrother and L. McElwee-White, Design, Synthesis, and Evaluation of CF3AuCNR Precursors for Focused Electron Beam-Induced Deposition of Gold, *ACS Appl. Mater. Interfaces*, 2019, **11**, 11976–11987.
8 A. T. M. Addaraidi, *An Investigation of Structural Motifs in Gold Complexes*, The University of Manchester, United Kingdom, 2018.
9 I. Utke, P. Hoffmann, B. Dwir, K. Leifer, E. Kapon and P. Doppelt, Focused electron beam induced deposition of gold, *J. Vac. Sci. Technol., B: Microelectron. Nanometer Struct.–Process., Meas., Phenom.*, 2000, **18**, 3168.
10 P. Nava, D. Hagebaum-Reignier and S. Humbel, Bonding of gold with unsaturated species, *ChemPhysChem*, 2012, **13**, 2090–2096.
11 P. Pyykkö and P. Zaleski-Ejgierd, Basis-set limit of the aurophilic attraction using the MP2 method: The examples of [ClAuPH3]2 dimer and [P(AuPH3)4]+ ion, *J. Chem. Phys.*, 2008, **128**, 124309.
12 S. G. Wang and W. E. Schwarz, Quasi-relativistic density functional study of aurophilic interactions, *J. Am. Chem. Soc.*, 2004, **126**, 1266–1276.
13 T. Yanai, D. P. Tew and N. Handy, A new hybrid exchange-correlation functional using the Coulomb-attenuating method (CAM-B3LYP), *Chem. Phys. Lett.*, 2004, **393**, 51–57.
14 F. Rabilloud, Structure and Stability of Coinage Metal Fluoride and Chloride Clusters (MnFn and MnCln, M 5Cu, Ag, Or Au; n 51–6), *J. Comput. Chem.*, 2012, **33**, 2083–2091.
15 J. Kopyra, F. Rabilloud, P. Wierzbicka and H. Abdoul-Carime, Energy-Selective Decomposition of Organometallic Compounds by Slow Electrons: The Case of Chloro(dimethyl sulfide)gold(I), *J. Phys. Chem. A*, 2021, **125**, 966–972.

16 L. Antes, S. Dapprich, G. Frenking and P. Schwerdtfeger, The Stability of Group 11 ClMCO complexes (M=Cu, Ag, Au), *Inorg. Chem.*, 1996, **35**, 2089–2096.
17 D. Sorbelli, L. Belpassi, F. Tarantelli and P. Belanzoni, Ligand Effect on Bonding in Gold(III) Carbonyl Complexes, *Inorg. Chem.*, 2018, **57**, 6161–6175.
18 D. Sorbelli, L. Belpassi and P. Belanzoni, Mechanistic Study of Alkyne Insertion into Cu–Al and Au–Al Bonds: A Paradigm Shift for Coinage Metal Chemistry, *Inorg. Chem.*, 2022, **61**, 21095–21106.
19 L. M. Reynard, C. J. Evans and M. C. L. Gerry, The Pure Rotational Spectrum of AuI, *J. Mol. Spectrosc.*, 2001, **205**, 344–346, DOI: 10.1006/jmsp.2000.8274.
20 C. J. Evans and M. C. L. Gerry, The Pure Rotational Spectra of AuCl and AuBr, *J. Mol. Spectrosc.*, 2000, **203**, 105–117, DOI: 10.1006/jmsp.2000.8150.
21 X. Li, Metalophilic Interaction in Gold Halide: Quantum Chemical Study of AuX (X = F-At), *J. Comput. Chem.*, 2014, **35**, 923–931.
22 M. Huth, F. Porrati, C. Schwalb, M. Winhold, R. Sachser, M. Dukic, J. Adams and G. Fantner, Focused electron beam induced deposition: A perspective, *Beilstein J. Nanotechnol.*, 2012, **3**, 597–619, DOI: 10.3762/bjnano.3.70.
23 W. F. van Dorp and C. W. Hagen, A critical literature review of focused electron beam induced deposition, *J. Appl. Phys.*, 2008, **104**, 081301, DOI: 10.1063/1.2977587.
24 I. Utke, P. Hoffmann and J. Melngailis, Gas-assisted focused electron beam and ion beam processing and fabrication, *J. Vac. Sci. Technol., B: Microelectron. Nanometer Struct.–Process., Meas., Phenom.*, 2008, **26**, 1197–1276, DOI: 10.1116/1.2955728.
25 N. Silvis-Cividjian and C. W. Hagen, Electron-Beam–Induced Nanometer-Scale Deposition, *Adv. Imaging Electron Phys.*, 2006, **143**, 1–235, DOI: 10.1016/s1076-5670(06)43001-9.
26 K. Höflich, R. B. Yang, A. Berger, G. Leuchs and S. Christiansen, The Direct Writing of Plasmonic Gold Nanostructures by Electron-Beam-Induced Deposition, *Adv. Mater.*, 2011, **23**, 2657–2661, DOI: 10.1002/adma.201004114.
27 S. Graells, S. Aćimović, G. Volpe and R. Quidant, Direct Growth of Optical Antennas Using E-Beam-Induced Gold Deposition, *Plasmonics*, 2010, **5**, 135–139, DOI: 10.1007/s11468-010-9128-9.
28 M. Mostafa, P. T. Shawrav, H. D. Wanzenboeck, M. Schinnerl, M. Stöger-Pollach, S. Schwarz and A. Steiger-Thirsfeld, Emmerich Bertagnolli Highly conductive and pure gold nanostructures grown by electron beam induced deposition, *Sci. Rep.*, 2016, **6**, 34003.
29 I. Utke, P. Swiderek, K. Höflich, K. Madajska, J. Jurczyk, P. Martinović and I. B. Szymańska, Coordination and organometallic precursors of group 10 and 11: Focused electron beam induced deposition of metals and insight gained from chemical vapour deposition, atomic layer deposition, and fundamental surface and gas phase studies, *Coord. Chem. Rev.*, 2022, **458**, 213851–213915.
30 W. F. v. Dorp, X. Wu, J. J. L. Mulders, S. Harder, P. Rudolf and J. T. M. D. Hosson, Gold Complexes for Focused-Electron-Beam-Induced Deposition, *Langmuir*, 2014, **30**, 12097–12105.
31 W. Kohn, A. D. Becke and R. G. Parr, Density Functional Theory of Electronic Structure, *J. Phys. Chem.*, 1996, **100**, 12974–12980, DOI: 10.1021/jp960669l.
32 A. D. Becke, *Modern Electronic Structure Theory, Part II Yarkony*, ed. D. R. Yarkony, World Scientific, Singapore, 1995, p. 1022.
33 T. Ziegler, Approximate density functional theory as a practical tool in molecular energetics and dynamics, *Chem. Rev.*, 1991, **91**, 651–667, DOI: 10.1021/cr00005a001.
34 B. P. Pritchard, D. Altarawy, B. Didier, T. D. Gibson and T. L. A. Windus, New Basis Set Exchange: An Open, Up-to-date Resource for the Molecular Sciences Community, *J. Chem. Inf. Model.*, 2019, **59**, 4814–4820.
35 M. J. Frisch, G. W. Trucks, H. B. Schlegel, G. E. Scuseria, M. A. Robb, J. R. Cheeseman, G. Scalmani, V. Barone, B. Mennucci, and *et al.*, *Gaussian 09*, Revision B.01, Gaussian, Inc., 2010.
36 M. E. Casida, C. Jamorski, K. C. Casida and D. R. Salahub, Molecular excitation energies to high-lying bound states from time-dependent density-functional response theory: Characterization and correction of the time-dependent local density approximation ionization threshold, *J. Chem. Phys.*, 1998, **108**, 4439–4449.
37 C. Adamo and D. Jacquemin, The calculations of excited-state properties with Time-Dependent Density Functional Theory, *Chem. Soc. Rev.*, 2013, **42**, 845.
38 F. Neese, Software Update: The ORCA Program System—Version 6.0, *Wiley Interdiscip. Rev.:Comput. Mol. Sci.*, 2025, **15**(2), e70019.
39 P. Schwerdtfeger, Relativistic Effects in Properties of Gold, *Angew. Chem., Int. Ed.*, 2003, **42**, 892–1895.
40 F. Weinhold, and J. E. Carpenter in *The Structure of Small Molecules and Ions*, 1988, pp. 227–236.
41 T. Lu and F. C. Multiwfn, A multifunctional wavefunction analyzer, *J. Comput. Chem.*, 2012, **33**, 580–592.
42 K. Kitaura and K. Morokuma, A new energy decomposition scheme for molecular interactions within the Hartree-Fock approximation, *Int. J. Quantum Chem.*, 1976, **10**, 325–340, DOI: 10.1002/qua.560100211.
43 T. Ziegler and A. Rauk, On the calculation of bonding energies by the Hartree Fock Slater method I. The transition state method, *Theor. Chim. Acta*, 1977, **46**, 1–10, DOI: 10.1007/BF02401406.
44 S. Dapprich and G. Frenking, Investigation of Donor-Acceptor Interactions: A Charge Decomposition Analysis Using Fragment Molecular Orbitals, *J. Phys. Chem.*, 1995, **99**, 9352–9362.
45 C. Morell, A. Grand and A. Toro-Labbe, New Dual Descriptor for Chemical Reactivity, *J. Phys. Chem. A*, 2005, **109**, 205–212.
46 B. Cordero, V. Gomez, A. E. Pletro-Prats, M. Reves, J. Echeverria, E. Cremades, F. Barragan and S. Alvarez, Covalent radii revisited, *Dalton Trans.*, 2008, 2832–2838.
47 S. Komeda, R. Takahashi and Y. Yamamoto, Trans Influence in Gold(I) Complexes, *Inorg. Chem.*, 2023, **62**, 14032–14040.

48 F. Rabilloud, Structure and Bonding in Coinage Metal Halide Clusters MnXn, M = Cu, Ag, Au; X = Br, I; n = 1−6, *J. Phys. Chem. A*, 2012, **116**, 3474–3480.
49 R. G. Parr and R. G. Pearson, Absolute Hardness: Companion Parameter to Absolute Electronegativity, *J. Am. Chem. Soc.*, 1983, **105**, 7512–7516.
50 R. G. Pearson, The Principle of Maximum Hardness, *Acc. Chem. Res.*, 1993, **26**, 250–255.
51 R. G. Pearson, Absolute Electronegativity and Hardness: Application to Inorganic Chemistry, *Inorg. Chem.*, 1988, **27**, 734–740.